



# Contact dynamics for a solid–solid reaction mediated by gas-phase oxygen: Study on the soot oxidation over ceria-based catalysts



Marco Piumetti<sup>a</sup>, Bart van der Linden<sup>b</sup>, Michiel Makkee<sup>b</sup>, Paolo Miceli<sup>a</sup>, Debora Fino<sup>a</sup>, Nunzio Russo<sup>a</sup>, Samir Bensaid<sup>a,\*</sup>

<sup>a</sup> Department of Applied Science and Technology, Politecnico di Torino, Corso Duca degli Abruzzi 24, 10129 Turin, Italy

<sup>b</sup> Catalysis Engineering, Department of Chemical Engineering, Faculty of Applied Sciences, Delft University of Technology, Julianalaan 136, 2628 BL Delft, The Netherlands

## ARTICLE INFO

### Article history:

Received 4 April 2016

Received in revised form 27 May 2016

Accepted 2 June 2016

Available online 4 June 2016

### Keywords:

Ceria

Soot–catalyst contact points

Accessible surface area

Soot oxidation

Nanostructured ceria

Nanocatalysts

## ABSTRACT

Ceria-based catalysts with different topological and textural properties have been prepared to study the role of the soot–catalyst contact on the soot oxidation reaction. The physico-chemical features of the catalysts have been investigated by means of complementary techniques, such as powder XRD, N<sub>2</sub> physisorption at −196 °C, optical microscopy at variable temperature, FESEM, TEM, and thermogravimetric analysis.

As a whole, the best catalytic activity has been obtained with the CeO<sub>2</sub>–nanocubes (denoted to as “Ce-NC”) because of their higher intrinsic reactivity. On the other hand, high-surface area materials prepared by the cerium nitrate decomposition (denoted to as “Ce-ND”) or hydrothermal route (CeO<sub>2</sub>–stars, referred to as “Ce-SAS”) resulted less effective toward the soot combustion, confirming the surface-sensitivity for this reaction.

Moreover, it has been proven a higher dependence of the oxidation activity on the catalyst-to-soot ratio (wt./wt.) for the nanostructured catalyst (Ce-NC) exhibiting the lowest BET specific surface area ( $S_{\text{BET}} = 4 \text{ m}^2 \text{ g}^{-1}$ ). On the other hand, the accessible (real) surface area, at variance of the BET surface area, seems to play a relevant role for this solid–solid reaction mediated by gas-phase oxygen.

© 2016 Elsevier B.V. All rights reserved.

## 1. Introduction

Recent legislation has introduced stringent particulate matter (PM) limits for vehicles, thus promoting the improvement of current technologies to satisfy the stated standards [1–4]. Among the different alternatives, the entrapment of particulates from exhaust gases by Diesel particulate filters (DPFs) has received much interest since its application by PSA in years 2000s, and has become widely applied in EU since 2008 with the introduction of Euro 4 standards [5–10].

The solid carbon (soot) that forms Diesel exhaust particulate can be burnt above 500 °C [9], whereas typical Diesel engine exhaust temperatures fall within the 200–500 °C range [10]. Therefore, solid catalysts are necessary to increase the oxidation rate of filter traps at low temperatures. Among the many oxidation catalysts designed since the 1980s, ceria-based catalysts appear to be the most promising candidates for DPFs due to their excellent redox behavior and high oxygen storage capacity (OSC) [11]. Moreover, the low cost

of ceria (as compared to noble metals) made CeO<sub>2</sub>–based materials particularly attractive for Diesel exhaust aftertreatment devices [1].

The feasibility of soot combustion depends to a great extent on the catalyst–soot contact conditions and it is, therefore, necessary to maximize the interactions between the catalyst surface and soot particles, both of which are solid components [12,13]. However, “tight” contact conditions are usually difficult to be obtained in real exhaust conditions because of the different orders of magnitude between soot and catalyst particle sizes. In order to consider the soot oxidation activity of various catalytic materials, two kinds of catalyst–soot contact conditions are mostly used for laboratory-scale studies [14,15]:

- “Loose” contact is usually obtained by gently shaking the catalyst–soot mixture with a spatula. Although the procedure is very short (it takes about 1–2 min), the established contact leads to reproducible results. The method, in fact, consents to homogenize the solid mixture, but still allows the two solid phases to be put in contact loosely. Neeft et al. [16] have shown that the soot–catalyst contact in a DPF is as loose as that of materials mixed roughly with a spatula.

\* Corresponding author.

E-mail address: [samir.bensaid@polito.it](mailto:samir.bensaid@polito.it) (S. Bensaid).

- “Tight” contact is achieved through a ball-milling (or a mortar) to obtain an intimate contact between the catalyst and soot. When soot is mixed with a catalyst by a ball-milling procedure, the oxidation rate is much higher than when soot and catalyst are mixed in “loose” contact. Moreover, this procedure maximizes the soot-catalyst contact points and then it is able to discriminate the surface reactivity better. On the other hand, it is less representative of the “real” contact conditions occurring in a catalytic trap.

As it is known, the contact between soot and catalyst particles is of great importance in the estimation of the soot oxidation kinetics and, nowadays, there is still a need to study soot-catalyst contact dynamics more realistically for designing highly effective materials, such as the nanostructured ceria-based catalysts. Thus, in order to increase the soot-catalyst interactions, different structures of ceria have been developed, such as nanofibers, stars, nanorods and, more recently, nanocubes [17–21].

In the present work, ceria-based materials with different topological and textural properties ( $\text{CeO}_2$ -nanocubes,  $\text{CeO}_2$ -stars and “classical”  $\text{CeO}_2$ , referred to as Ce-NC, Ce-SAS and Ce-ND, respectively) have been prepared to investigate the soot-catalyst contact conditions and their role toward the soot oxidation reaction. The physico-chemical features of the prepared catalysts have been investigated by complementary techniques.

## 2. Experimental

### 2.1. Preparation of the samples

A detailed description of the procedures used for the preparation of the three catalysts is reported elsewhere [19,20]. Briefly, ceria nanocubes (denoted as “Ce-NC”) were prepared via the hydrothermal method: proper amounts of NaOH (24 g) and  $\text{Ce}(\text{NO}_3)_3 \cdot 6\text{H}_2\text{O}$  (2.2 g) were dissolved in 35 mL and 5 mL of bi-distilled water, respectively. The two solutions were then mixed together and stirred for 1 h to obtain a milky slurry. The final mixture was transferred to an autoclave (150 mL) and then aged at 165 °C for 24 h. The fresh precipitate was washed and dried at 60 °C overnight. Finally, the powder was calcined at 550 °C for 4 h.

$\text{CeO}_2$  self-assembled stars (denoted as “Ce-SAS”) were prepared via a hydrothermal route in a batch stirred-tank reactor [19]. The first step consists in dropping  $\text{CeCl}_3 \cdot 7\text{H}_2\text{O}$  (0.2 M) in cetyl trimethylammonium bromide (CTAB) aqueous solution (0.01 M); subsequently, urea (80 mmol) was added to the mixture to get a 4:1 ratio between urea and cerium salt. The obtained solution was stirred for 30 min at room temperature. Next, the final solution must stay in the stirred tank for 24 h at 120 °C, and then cooling for 24 h to get a white precipitate. The latter was dried at 60 °C for 24 h and calcined at 600 °C for 4 h.

“Classical”  $\text{CeO}_2$  (denoted as “Ce-ND”) was obtained through the thermal decomposition of  $\text{Ce}(\text{NO}_3)_3 \cdot 6\text{H}_2\text{O}$  (dried initially at 100 °C for 5 h) by calcination at 500 °C for 5 h. All calcinations have been carried out in static air.

### 2.2. Characterization of the catalysts

The powder X-ray diffraction patterns were collected on a X'Pert Philips PW3040 diffractometer using  $\text{Cu K}\alpha$  radiation ( $2\theta$  range = 20°–70°). The diffraction peaks were indexed according to the Powder Data File database (PDF 2000, International Centre of Diffraction Data, Pennsylvania).

The BET specific surface area ( $S_{\text{BET}}$ ) and total pore volume ( $V_p$ ) were determined by  $\text{N}_2$  physisorption at –196 °C on a Micrometrics ASAP 2020 instrument. Prior to the analyses, the samples were

outgassed at 200 °C for 2 h to remove water and other atmospheric contaminants. The specific surface area of the samples was calculated using the BET method.

Sample morphology was investigated by means of a field emission scanning electron microscope (FESEM Zeiss MERLIN, Gemini-II column) and Transmission Electron Microscopy (TEM, Jeol JEM 3010 operating at 200 kV).

Thermogravimetric analyses (TGA) were performed through a Mettler-Toledo instrument (TGA/SDTA851e). Printex-U was used as model soot. The ceria+soot (3 wt.%) mixture was obtained by shaking the container for 1 min. Samples were heated to 800 °C at 10 °C min<sup>–1</sup> flowing air (100 mL min<sup>–1</sup>). The weight loss was recorded *versus* temperature. Optical microscopy analyses at variable temperature were performed with a ZEISS SteREO Discovery.V8 microscope using an objective of 80x linear magnification. The image generated (250×, 2080 × 1540 pixels) by the microscope was recorded by AxioCam ICc3 camera and transferred to a computer using the AXIOVision software. The sample was placed on a 7 mm diameter quartz disc and placed in a high temperature Linkam Stage TS1500 *in-situ* cell sample holder, as schematized in Fig. 1-top. Air flow rate was 10 mL min<sup>–1</sup>. A temperature controller Linkam TMS 93 was used to carry out temperature programmed experiments. Image observations were done with the optical microscope (Fig. 1-bottom) at the increase of temperature up to 1000 °C. The heating rate was approximately 30 °C min<sup>–1</sup>.

The comparison between TGA and Linkam stage tests is not direct, since the soot oxidation temperatures recorded by the microscope camera do not match with the weight loss curves shown in the corresponding TGA plots. The shift in temperature, around 250 °C for each catalyst sample, can be explained by: i) the design of the Linkam stage, entailing that the heating element temperature differs from the one of the soot-catalyst sample; ii) the difference in heating rate.

### 2.3. Catalytic activity tests

The soot combustion activity of the catalysts was measured by means of temperature programmed oxidation (TPO). Tests were carried out in a fixed-bed micro-reactor (a quartz U-tube, with an inner diameter of 4 mm, heated by an electric, PID-regulated furnace). An oxidizing atmosphere containing 50% air and 50%  $\text{N}_2$  was fed at a constant rate of 100 mL min<sup>–1</sup> to the reactor. The catalytic bed was prepared by mixing 5 mg of carbon soot, 45 mg of powdered catalyst, and 150 mg of inert silica (soot/catalyst = 5/45 wt./wt.). The mixtures were prepared using two different methods to simulate the “loose” and “tight” contact conditions, as described elsewhere (*vide supra*) [11]. In order to evaluate the activities for various soot-to-catalyst ratios in “loose” contact conditions, further soot-catalyst mixtures were prepared with the following ratios: 9/41, 15/35, 20/30 wt./wt. (soot-catalyst mixture = 50 mg). The reaction temperature was measured with a thermocouple placed 5 mm above the catalytic bed, while the oven temperature was controlled by means of a PID-regulated system and varied from 200 to 700 °C at a 5 °C min<sup>–1</sup> rate. The  $\text{CO}_x$  concentrations in the outlet gas were measured via NDIR analyzers (ABB).

## 3. Results and discussion

### 3.1. Textural and morphological properties of the catalysts

Table 1 summarizes the main textural properties of the prepared samples, derived from both  $\text{N}_2$  physisorption at –196 °C and X-ray diffraction patterns.

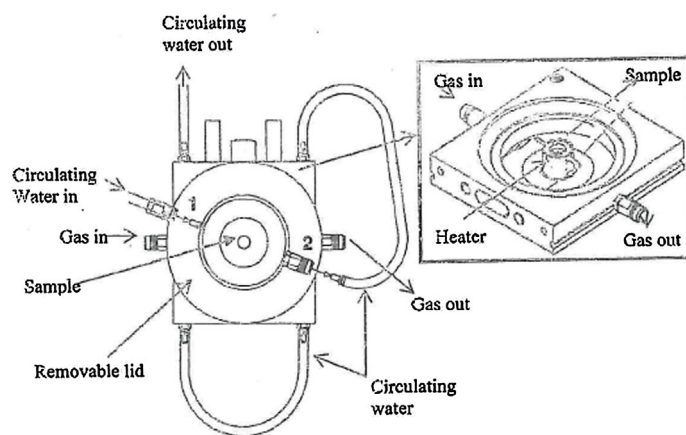


**Fig. 1.** Linkam Stage TS1500 *in-situ* cell sample holder (top) and ZEISS SteREO Discovery.V8 microscope (bottom) used for the optical microscopy experiments at variable temperature.

**Table 1**

Textural properties of the prepared Ceria-based catalysts, as obtained from  $N_2$  physisorption at  $-196^\circ\text{C}$  and X-ray diffraction patterns [19,20].

Catalyst	$S_{\text{BET}}$ ( $\text{m}^2 \text{g}^{-1}$ )	$V_p$ ( $\text{cm}^3 \text{g}^{-1}$ )	Crystallite size (nm)
Ce-NC	4	0.01	54
Ce-SAS	124	0.08	10
Ce-ND	72	0.20	7–35

Fig. 2 shows the XRD diffractograms for the samples: they exhibit similar patterns referring to cubic fluorite structure, marked by the existence of (111), (200), (220), (311), (222), and (400) planes [19–22]. The Scherrer's equation was employed to estimate the crystallite sizes: for the Ce-NC sample the average crystal size is about 54 nm, whereas the Ce-SAS has the smallest crystal size (ca. 10 nm); finally, the Ce-ND catalyst shows crystallites with dimensions between 7 and 35 nm.

The BET surface areas and total pore volumes, obtained from  $N_2$  physisorption measurement at  $-196^\circ\text{C}$ , are very low for the Ce-NC

sample ( $S_{\text{BET}} = 4 \text{ m}^2 \text{g}^{-1}$  and  $V_p = 0.01 \text{ cm}^3 \text{g}^{-1}$ ). In contrast, both the Ce-SAS and Ce-ND exhibit better textural properties, as reported in Table 1.

FESEM images for the Ce-NC, Ce-SAS and Ce-ND samples are shown in Fig. 3. The three micrographies show the characteristic morphologies of the prepared materials (cubes, stars, and agglomerates, respectively). Nanocubes are present in the size range of 50–200 nm, whereas the Ce-SAS sample comprises of self-assembled agglomerates (non-convex structures), which size can vary from hundreds of nanometers up to few micrometers (the average diameter is around  $1 \mu\text{m}$ ). Finally, the Ce-ND sample exhibits foamy agglomerates (in the 50–200 nm range) of small particles.

TEM images of the Ce-NC sample show the presence of truncated nanocubes with (100)-type planes and additional (110) surfaces (highly reactive) at their truncated corners (Fig. 4a). The equilibrium shape of such nanocubes is determined by the Wulff rule [23], according to which the convex envelope of planes (perpendicular



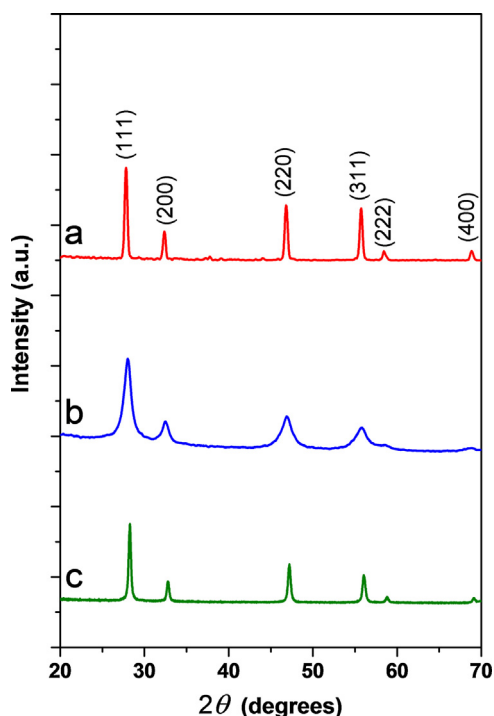


**Fig. 2.** Powder wide-angle XRD patterns of the a) Ce-NC, b) Ce-SAS, and c) Ce-ND samples. Adapted from [19,20].

to the surface normal) minimizes the surface energy for a given enclosed volume [24]. The particles exhibit cuboctahedral shapes with an average size of about 50 nm. The micrograph reported in Fig. 4b shows a nanoparticle oriented along the (100) direction with (100)-type planes, as reflected by the Fourier transform image (inset). As shown in Fig. 4c and d, the Ce-SAS sample consists in arrays of rods (star-like morphology) with relatively uniform diameters (ca. 500 nm). These micro-aggregates preferentially expose (310), (100), and (110) planes [25]. Finally, TEM images of the Ce-ND sample (Fig. 4e and f) show the presence of non-uniform particles of ca. 10–50 nm, exposing mainly (111)-type planes (inter-reticular distance = 0.31 nm).

### 3.2. FESEM study on the soot-catalyst mixtures

Fig. 5 shows FESEM micrographes at different levels of magnifications for the soot-catalyst mixtures prepared in “loose” contact conditions (soot/catalyst = 5/45 wt./wt.). An effective soot-catalyst interaction appears for the soot/Ce-NC mixture (Section A): the nanocubes are readily accessible to soot particles since they themselves are distributed in a spatially uniform manner into the solid mixture. Isolated phases of either soot or catalyst do not appear and the Ce-NC surfaces are mostly covered by soot aggregates. This confirms that (100) and (110)-type planes of the Ce-NC catalyst would be well-accessible to soot during the catalytic reaction despite the low textural properties of this catalyst.

Conversely, self-assembled  $\text{CeO}_2$  stars-like shapes should exhibit promising results for the incorporation of soot into the cavities because of their non-convex 3-D structures. However, soot particles form large aggregates (up to 1  $\mu\text{m}$ ) and then soot and Ce-SAS phases are partially segregated (Section B). In other words, the accessible (real) surface area for the Ce-SAS material is much lower than the specific surface area measured by the BET method. Similarly, soot agglomerates poorly dispersed in the mixture appear in large extent for the soot-Ce-ND mixture (Section C). Thus, although the gap between the accessible and BET surface area is little for

many catalytic processes (i.e. solid-gas or solid-liquid reactions), it may become significant for solid–solid reactions mediated by gas phase.

### 3.3. TGA experiments

The thermogravimetric analysis provides useful information from the mass-temperature plots, such as the temperature of the maximum oxidation rate ( $T_0$ ) and the temperature at which soot oxidation begins ( $T_{\text{onset}}$ ). Thus, the mass reduction curves for either the inert SiC-soot or soot-catalyst mixtures are comparatively shown in Fig. 6. Using SiC as support, the uncatalysed soot combustion (referred to as “Printex-U”) occurs between 500 and 650 °C, with  $T_0$  at ca. 620 °C. On the other hand, different reduction trends appear for the soot-catalyst mixtures under “loose” contact conditions. In particular, the Ce-NC catalyst exhibits the lowest oxidation temperature ( $T_0 = 470$  °C), thus reflecting the highest oxidation activity. A shoulder appears at ca. 530 °C because of the soot oxidation by the lower intrinsic reactivity of the exposed planes and weaker soot-to-catalyst interactions. According to our previous work [20], indeed, the activity depends on various surface orientations, namely in the sequence (110) > (100) > (111), that is to say it is strongly influenced by the surface structure. This multimodal shape of the oxidation curve is also present in the later presented results of catalyst activity with flowing reacting gas.

On the other hand, the Ce-SAS sample does not significantly reduce the  $T_0$  value with respect to the uncatalysed soot oxidation ( $T_0 = 616$  °C), although it affects the onset temperature due to its high BET surface area, as described elsewhere [19,25]. Moreover, several peaks appear in the low-temperature range (<350 °C) as consequence of the high BET surface area of this catalyst. More specifically, these peaks are ascribed to  $\text{CO}_2$  desorption from the microporous volume of the Ce-SAS catalyst [25], and not to any catalytic-related activity, as elucidated by temperature programmed desorption experiments carried out till 200 °C in  $\text{N}_2$  environment [25]. A similar pattern can be observed for the Ce-ND sample, although the latter shows better performance in terms of  $T_0$  (= 565 °C). Coherently, the TPO activity measurements reported in [19,25], although they differ in terms of absolute temperature from the here-reported TGA analysis, show that the Ce-SAS sample provides no significant shift of the peak oxidation temperature versus “conventional” ceria obtained by the Solution Combustion Synthesis (Ce-SCS in [25], similar to the here presented Ce-ND).

### 3.4. Optical microscopy at variable temperature

Fig. 7 shows the optical microscopy images for the soot-catalyst mixtures prepared in “loose” contact conditions, along with Printex-U. It must be pointed out that the absolute temperatures here recorded are higher than the ones obtained in a closed system (such as in a TGA or TPO experiment), since the optical microscopy observation brings along heat dispersion to the environment. However, optical microscopy experiments are essential for this study on the contact dynamics soot-catalyst, since the temperature at which a phenomenon occurs can be directly correlated to its visualization.

In the Supporting information, the *in-situ* visualization of soot oxidation is available as movie.

According to micrographs recorded at different temperatures, the uncatalysed soot combustion (Printex-U) begins at ca. 700 °C and proceeds up to 950 °C. A similar trend can be observed for the soot combustion over the Ce-SAS catalyst. Lower temperatures appear for the “Ce-ND + Printex-U” system (soot combustion occurs in the 400–900 °C range), thus reflecting a higher reactivity of the Ce-ND catalyst. Moreover, poorly dispersed soot aggregates (= spatially segregated) appear for the “Ce-SAS + Printex-U” and “Ce-ND + Printex-U” mixtures. Conversely, the Ce-NC catalyst ex-

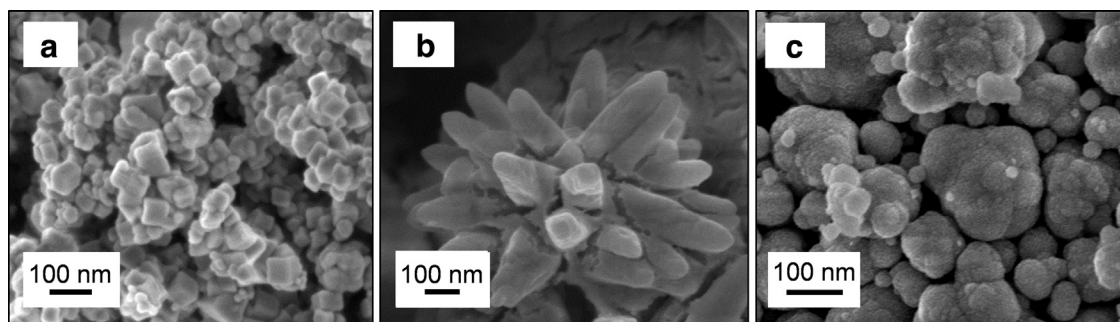


**Fig. 3.** FESEM images of the a) Ce-NC, b) Ce-SAS, and c) Ce-ND samples.

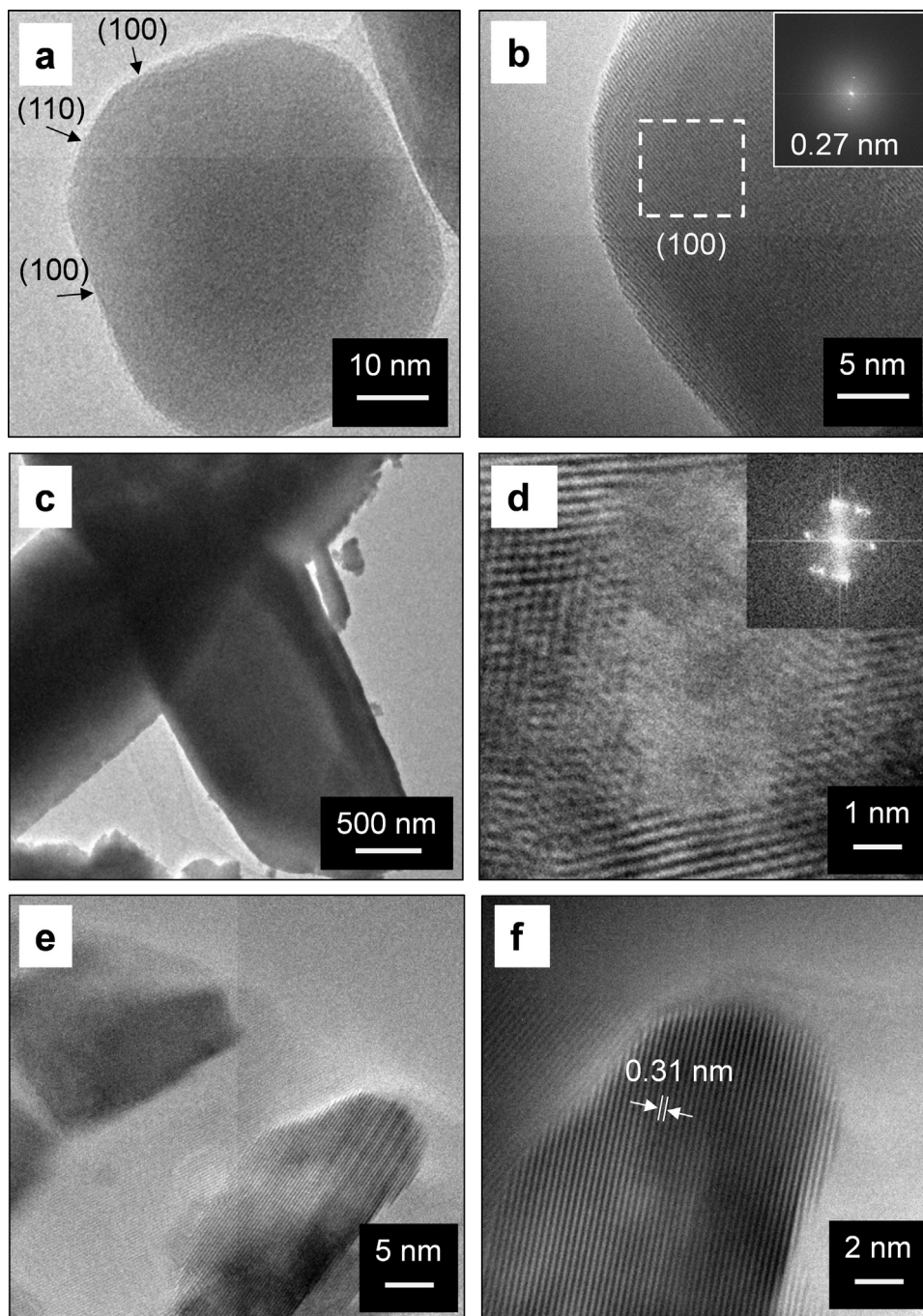


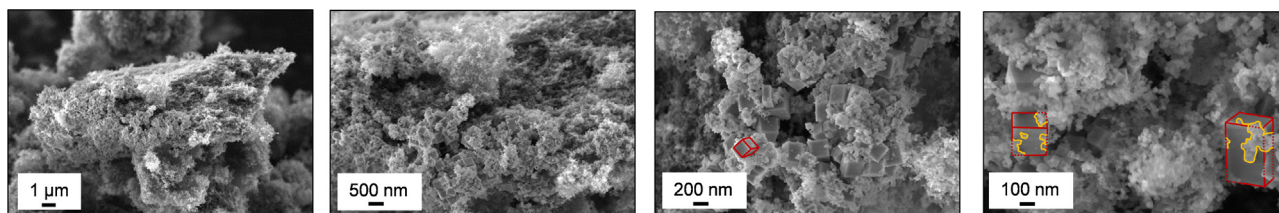
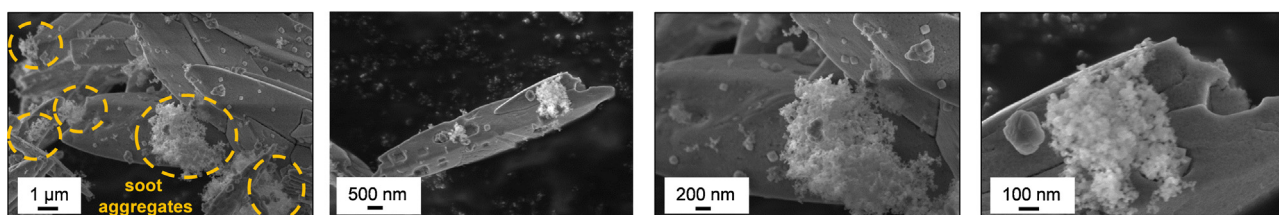
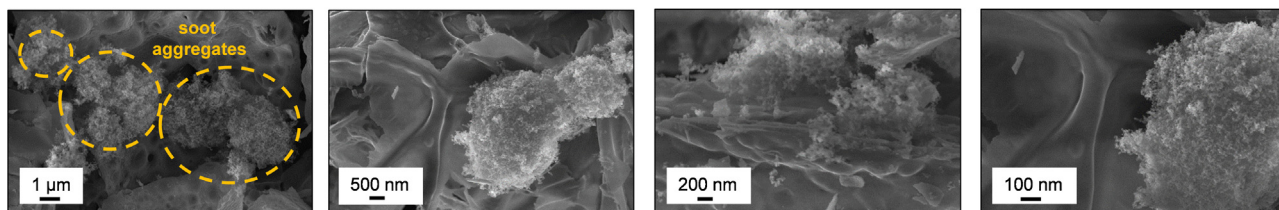
**Fig. 4.** TEM images of the Ce-NC (a and b), Ce-SAS (c and d), and Ce-ND (e and f) samples. Adapted from [19,20].



**Table 2**

Results of the CO<sub>2</sub> peaks deconvolution for the Ce-NC, Ce-SAS and Ce-ND catalysts under “loose” contact conditions (5/45 soot-to-catalyst weight ratio). The areas corresponding to the peaks are expressed in terms of peak temperature and % of the total area below the CO<sub>2</sub> curve.

Catalyst	T <sub>peakI</sub> (°C)	A <sub>peakI</sub> (%)	T <sub>peakII</sub> (°C)	A <sub>peakII</sub> (%)	T <sub>peakIII</sub> (°C)	A <sub>peakIII</sub> (%)
Ce-NC	431	31.3%	493	60.2%	582	8.5%
Ce-SAS	–	–	522	52.5%	582	47.5%
Ce-ND	–	–	529	72.2%	587	27.8%

**A****B****C**

**Fig. 5.** FESEM images of soot-catalyst mixtures prepared in “loose” contact conditions (soot/catalyst = 4/45 wt./wt.) for the Ce-NC (Section A), Ce-SAS (Section B), and Ce-ND (Section C) samples.

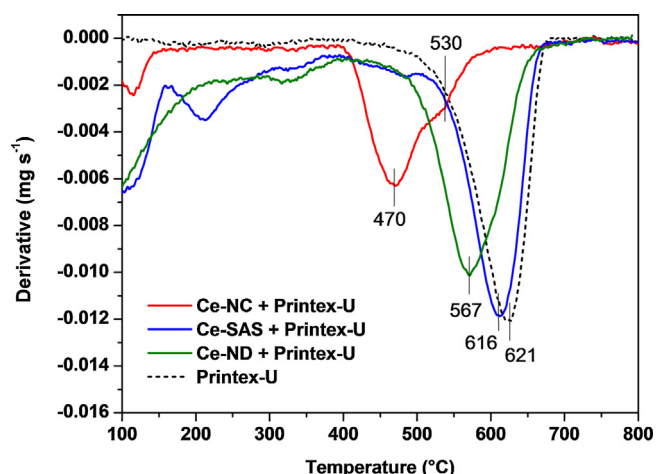


**Fig. 6.** TGA profiles of different soot-catalyst mixtures prepared in “loose” contact conditions.

exhibits the highest activity: soot combustion takes place at lower temperatures, reflecting the higher intrinsic reactivity of the CeO<sub>2</sub> nanocubes [20] and better homogeneity for the “Ce-NC+Printex-U” mixture. The gap existing between the accessible surface area and the BET surface area appears a constraint for the performances

of Ce-SAS and Ce-ND catalysts. In fact, the accessible surface area seems to play a key role for this solid–solid reaction mediated by gas-phase oxygen.

### 3.5. Catalytic activity tests

The prepared catalysts were tested for the soot combustion by means of TPO runs. As expected Fig. 8 shows the soot conversion to CO<sub>x</sub> as function of temperature over the prepared catalysts and Printex-U (without catalyst) in “loose” (Fig. 8A) and “tight” contact (Fig. 8D), respectively. All catalysts exhibited positive soot conversion trends for an increasing reaction temperature, and they were able to lower the light-off temperatures, as well as the temperatures of the maximum oxidation rate, compared to Printex-U. On one hand, soot conversion values achieved in “tight” contact conditions were better than those obtained in “loose” contact, as a consequence of the stronger soot-catalyst interactions (oxidation at more contact points) and more effective transport phenomena. As a whole, Ce-NC appears to be the most promising catalyst due to the abundance of highly reactive (100) and (110) surfaces. Worse performances (in terms of T<sub>50%</sub> and T<sub>90%</sub> values) were achieved for the two high-surface area samples. These results are in fair agreement with the recent literature, according to which ceria-based nanocatalysts, exhibiting highly reactive surfaces, may lead

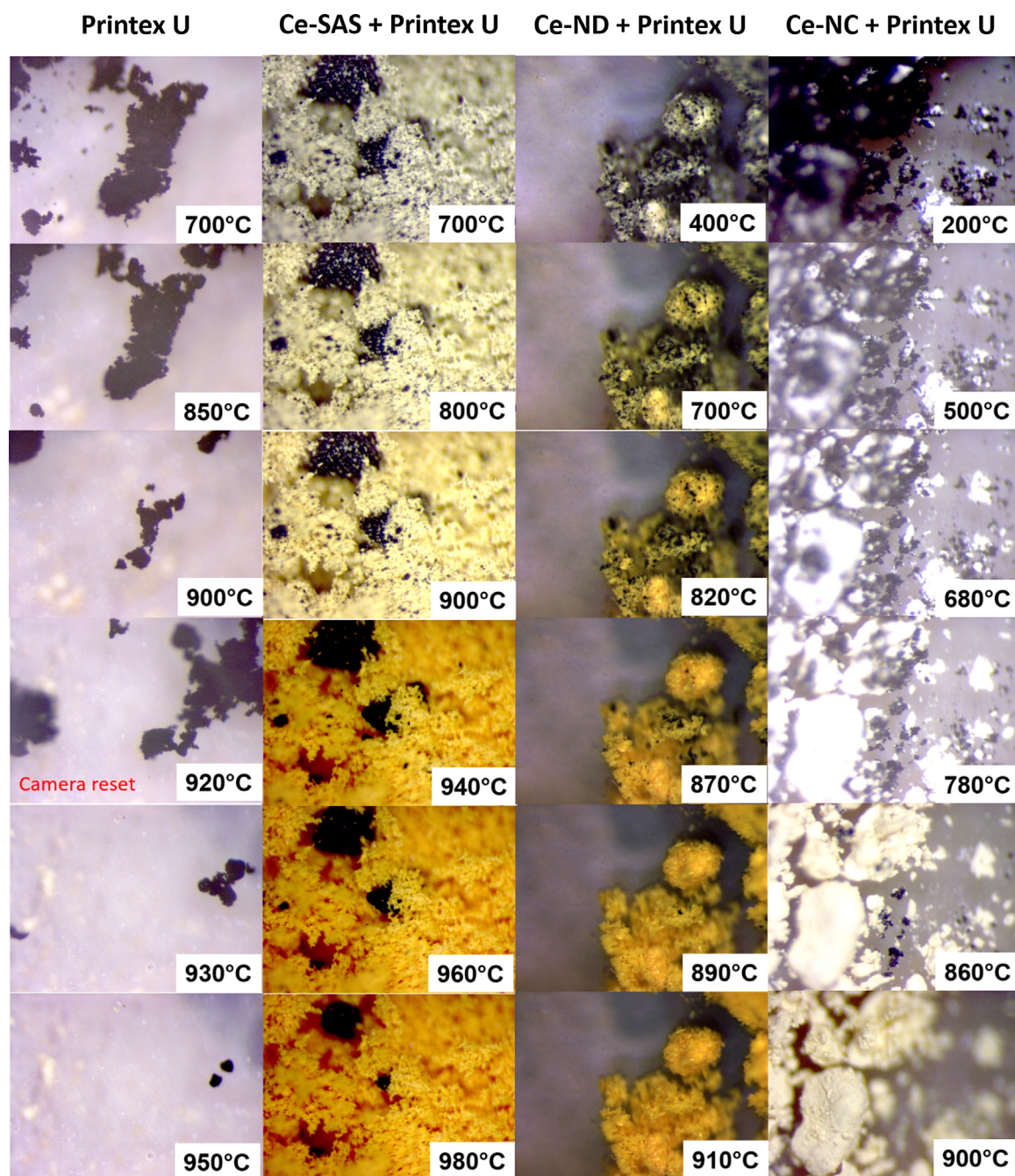


**Fig. 7.** Optical microscope images of different soot-catalyst mixtures, under programmed temperature increase. Image size: 1 mm. Temperature tags refer to the heating element temperature.

to a high oxidation activity despite their low BET surface areas [11,20,26].

At low temperatures, however, the surface-insensitivity would be due to the presence of adsorbed species (e.g. hydroxyl groups, inert molecules, etc.) which weaken the reactant-catalyst surface interactions or are inactive in the oxidation reaction, in both cases masking the catalyst surface [20,27].

The soot conversion curves for these catalysts depend on several factors, including their intrinsic reactivity, textural properties, and soot-catalyst contact. In fact, multimodal distributions of  $\text{CO}_2$  (Figs. 8B and E) and CO (Figs. 8C and F) appear over the whole temperature range. In particular, peaks related to the formation of  $\text{CO}_x$  in the 400–550 °C range reflect the kinetic effects, whereas at higher

temperatures radical mechanisms take place [28–30], mainly due to non-catalytic soot oxidation. In “tight” contact all catalysts produce  $\text{CO}_x$  at low temperatures (<550 °C), whereas the peaks related to  $\text{CO}_x$  formed via radical mechanisms occur in “loose” contact condition. This finding confirms that soot and catalyst particles are partially segregated in “loose” contact, especially for the Ce-ND and Ce-SAS catalysts.

For both “loose” and “tight” contact conditions, the most active catalyst (Ce-NC) exhibits intense peaks of  $\text{CO}_2$  and CO at low temperature, at variance of the Ce-ND and Ce-SAS samples, which are less catalytically active. In agreement with both TGA and optical microscopy characterizations (*vide supra*), the Ce-ND catalyst appears more reactive than Ce-SAS. On the other hand, the Ce-SAS



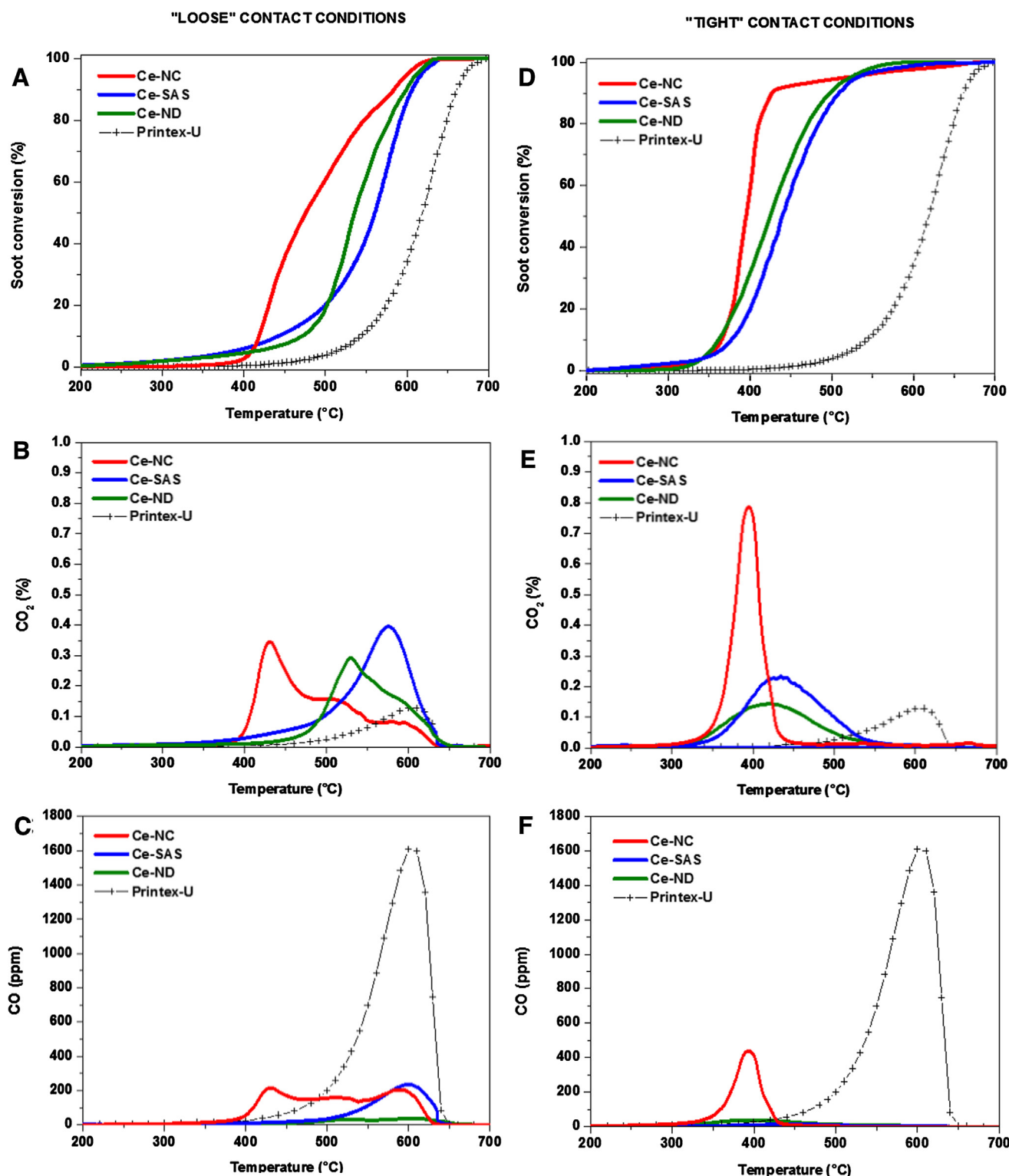


**Fig. 8.** Soot conversions (%) (A and D), CO<sub>2</sub> concentrations (B and E), and CO concentrations (C and F) over the prepared catalysts (5/45 soot-to-catalyst weight ratio) under "loose" (first column) and "tight" (second column) contacts.

catalyst exhibits superior soot conversion values at low temperature and in "loose" contact ( $T_{10\%} = 443$  and  $473$  °C for Ce-SAS and Ce-ND, respectively), as a consequence of the higher BET surface area. This behavior is in fair agreement with literature [19,25]. It is worth mentioning that, although Ce-NC appears to be the most active catalyst among the ones here investigated, its selectivity to

CO<sub>2</sub> is lower than the one of Ce-SAS and Ce-ND. Hence, Ce-NC possesses a very low  $S_{BET}$  ( $4 \text{ m}^2/\text{g}$ ), while Ce-SAS and Ce-ND have a much higher one ( $124$  and  $74 \text{ m}^2/\text{g}$ , respectively). As a result, Ce-SAS and Ce-ND are more effective towards CO oxidation, which is directly influenced by the BET surface, fully accessible to the CO molecule.



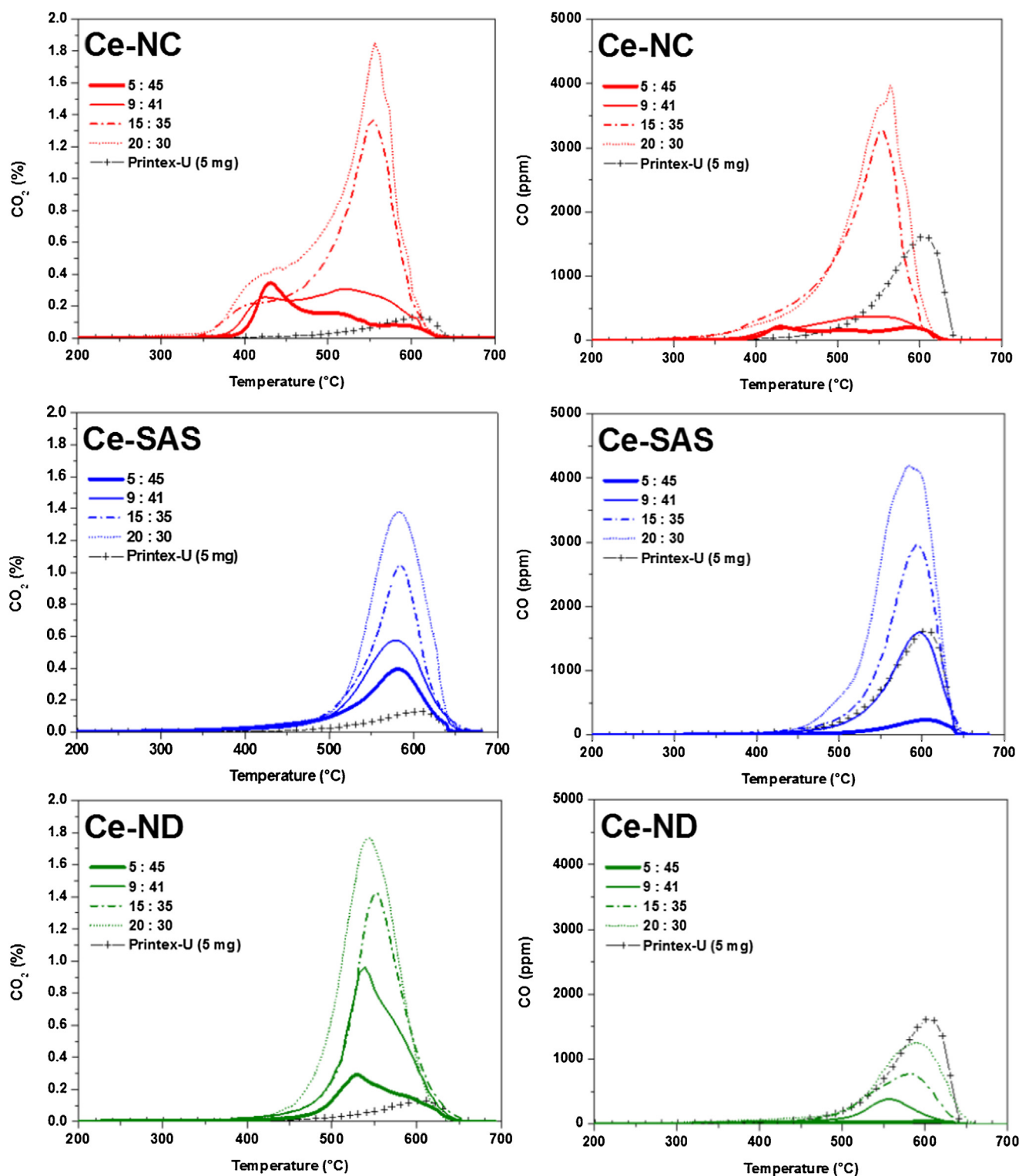
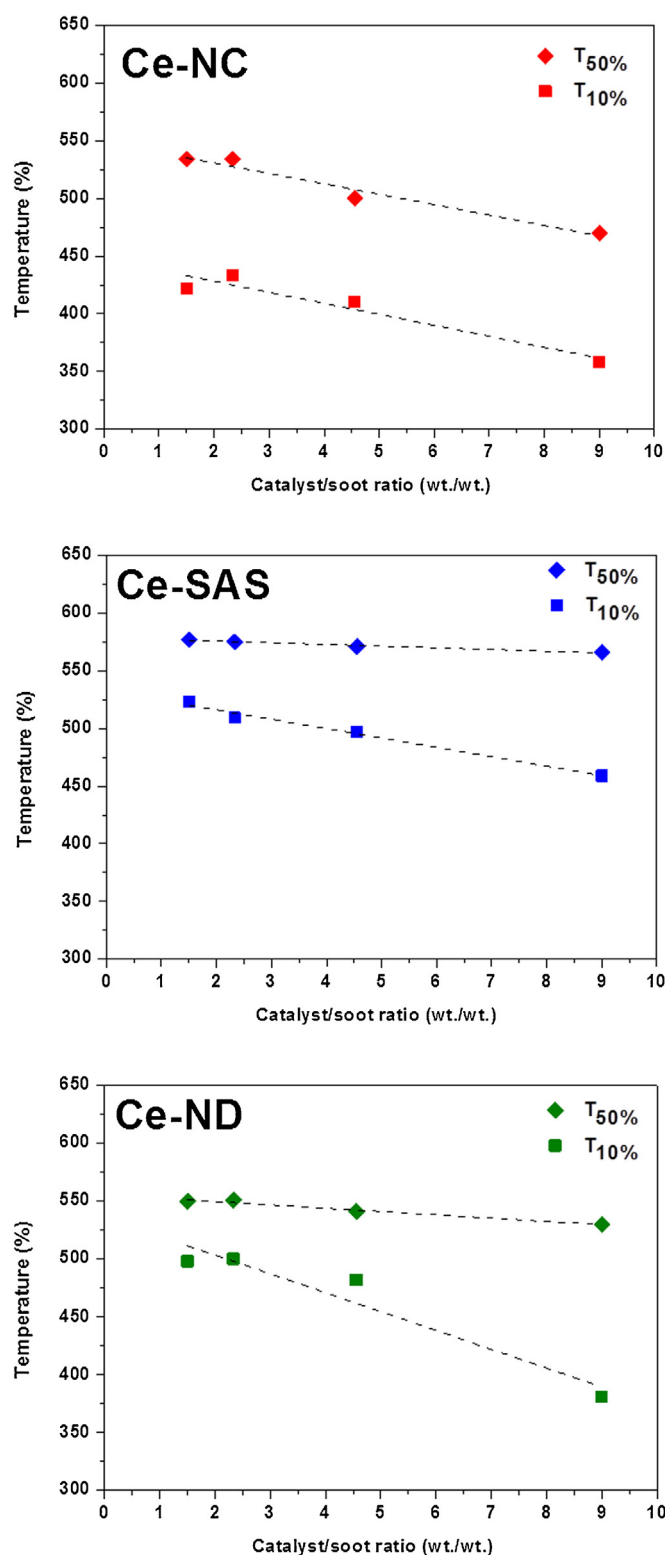


Fig. 9. CO<sub>2</sub> and CO concentrations over the Ce-NC, Ce-SAS, and Ce-ND catalysts at different soot-to-catalyst weight ratios (namely, 5/45, 9/41, 15/35 and 20/30) under “loose” contact conditions.

Fig. 9 compares the catalytic performances in “loose” contact for the mixtures with various soot-to-catalyst ratios (namely, 5/45, 9/41, 15/35, and 20/30 wt./wt.). As expected, at higher soot-to-catalyst ratios the peaks shift toward a higher temperature range, as well as the relative peak intensities, decrease at low temperatures. Another effect is the decrease of the CO<sub>2</sub> selectivity at higher

soot-to-catalyst ratios, as can be inferred by the decreasing CO<sub>2</sub> to CO ratio for higher soot content.

The dependence of the catalytic activity on the soot-to-catalyst ratio is greater for the Ce-NC sample ( $T_{\text{peakCO}_2} = 432$  and  $556^\circ\text{C}$  for 5/45 and 20/30 wt./wt., respectively;  $\Delta T_{\text{peakCO}_2} = 124^\circ\text{C}$ ), with respect to the high-surface-area samples ( $\Delta T_{\text{peakCO}_2} = 14$  and  $4^\circ\text{C}$  for Ce-SAS and Ce-ND). The kinetic phenomena for both the Ce-



**Fig. 10.** Temperatures at which 10% and 50% soot conversions ( $T_{10\%}$  and  $T_{50\%}$ , respectively) are reached as a function of the catalyst-to-soot ratios (wt./wt.).

SAS and Ce-ND catalysts take place at higher temperatures because of their lower intrinsic reactivity, and this makes the discrimination between the catalytic (redox mechanisms) and “non-catalytic” (radical mechanisms) contribution a particularly difficult task. A low dependence of the oxidation activity on the soot-to-catalyst ratio can be observed especially for Ce-SAS.

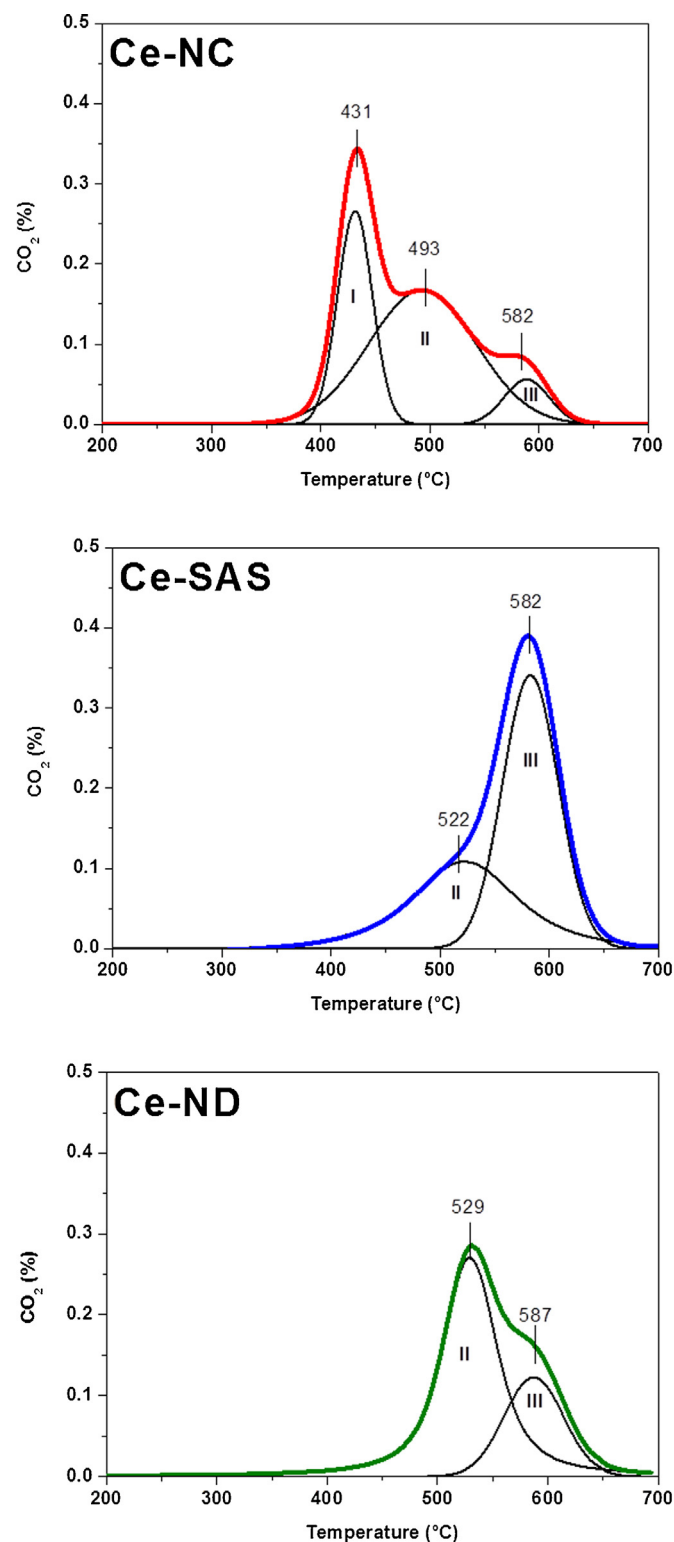


**Fig. 11.**  $CO_2$  peaks deconvolution for the Ce-NC, Ce-SAS, and Ce-ND catalysts (5/45 soot-to-catalyst weight ratio) under “loose” contact conditions.

Fig. 10 plots the onset-temperatures ( $T_{10\%}$ ) and half-conversion temperatures ( $T_{50\%}$ ) for the prepared catalysts as a function of the catalyst/soot values (wt./wt.) in “loose” contact conditions. As expected [31], both the  $T_{10\%}$  and  $T_{50\%}$  decrease at increasing catalyst/soot values. However, the onset temperature appears more sensitive than the half-conversion temperature, to variations in the catalyst-to-soot ratios, since  $T_{10\%}$  mainly depends on

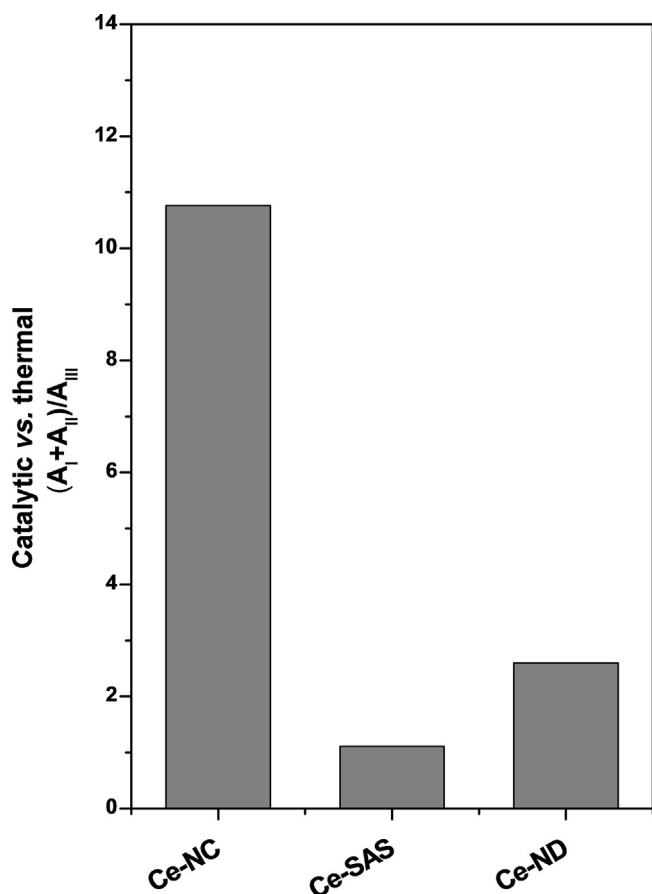


**Fig. 12.** Ratios of the peak areas  $(A_I + A_{II})/A_{III}$  obtained from the  $\text{CO}_2$  peaks deconvolution for the prepared catalysts under “loose” contact conditions (5/45 wt./wt. soot-to-catalyst ratio).  $(A_I + A_{II})/A_{III}$  values should reflect the catalytic *versus* thermal contribution for the soot combustion.

the share of soot that gets oxidized catalytically (the latter being directly affected by the catalyst-to-soot ratio). In particular, the  $T_{10\%}$  value achieved at the highest catalyst-to-soot ratio (namely, 9 = 45/5 wt./wt.) should reflect the intrinsic reactivity of the catalysts (in the sequence Ce-NC > Ce-ND > Ce-SAS).

For lower catalyst/soot values, the soot-to-catalyst contact would play a greater effect on the oxidation activity. The effect of the soot-to-catalyst contact can be analyzed through the slope of the  $T_{10\%}$  curve vs. catalyst-to-soot ratio: the steepest curve corresponds to the highest dependency of the oxidation activity to the soot-catalyst contact. Ce-SAS catalyst has a low sensitivity to  $T_{10\%}$  because of its low fraction of soot being oxidized catalytically; conversely, Ce-NC and Ce-ND have a stronger dependency on the catalyst-to-soot ratio (based on the  $T_{10\%}$  curve's slope), although the latter seems to worsen its oxidation activity faster than that of the former. This is maybe due to a lower surface of Ce-ND catalyst being accessible to the soot particles, *i.e.* higher segregation of soot aggregates for Ce-ND than for Ce-NC samples. Hence, the accessible area depends mainly on the morphology of the catalyst, rather than on its BET specific surface, whose area is much larger for Ce-ND than for Ce-NC.

Finally, the  $T_{50\%}$  values for the Ce-NC catalyst are also particularly sensitive to the catalyst/soot values, denoting that the amount of soot catalytically oxidized is a considerable share even at high catalyst-to-soot ratios, further confirming a high intrinsic reactivity of this material (low  $T_{50\%}$  compared to the other materials).

Fig. 11 shows the  $\text{CO}_2$  peaks' deconvolution for the Ce-NC, Ce-SAS, and Ce-ND catalysts during the soot combustion in “loose” contact conditions (soot-to-catalyst ratio = 5/45 wt./wt.). For the

Ce-NC catalyst three peaks appear at 431, 493, and 582 °C. These signals, referred to as “peaks I, II, and III”, respectively, correspond to the  $\text{CO}_2$  production through different phenomena, in agreement with the literature [28–30]. Specifically, Golodets [29] has classified the oxidation mechanisms as function of temperature, according to which surface redox-cycles occur in the 300–500 °C range, whereas they are replaced at higher temperatures by radical processes in the gas phase. Similarly, Bueno-López et al. [30] have shown that lattice oxygen is the “active oxygen” for soot oxidation at moderate temperatures (350–500 °C). Therefore, both the peaks I and II would reflect the  $\text{CO}_2$  produced via surface redox-mechanisms, whereas the peak III can be attributed to  $\text{CO}_2$  production by radical mechanisms (free-radicals in the gas phase). The fact that peak III occurs earlier than that in the absence of catalyst (*e.g.* see Fig. 8B) is due to the fostering effect of the formerly oxidized soot, which increases the temperature of the catalytic bed with respect to the inlet temperature (reported in the  $x$  axis), and self-promotes the oxidation reaction.

As reported in Table 2, the peaks I and II exhibit higher relative areas, as compared to the peak III, thus confirming the high reactivity for the Ce-NC catalyst. Conversely, a lower activity is achieved for both Ce-SAS and Ce-ND materials, exhibiting only two signals at 522–529 °C (peak II) and at 582–587 °C (peak III), whereas the peak I does not appear. As a result, peak III, which is attributed to a nearly uncatalyzed reaction, constitutes only 8.5% of total soot oxidation for the Ce-NC catalyst, while reaches 47.5% and 27.8% for the Ce-SAS and Ce-ND materials, respectively. Therefore, catalytic *versus* thermal contribution has been estimated for these catalysts by the ratios of the peak areas  $(A_I + A_{II})/A_{III}$  obtained from the  $\text{CO}_2$  peaks deconvolution (Fig. 12). Interestingly, the catalytic contribution for the Ce-NC catalyst is about twelve times greater than the thermal one, thus confirming the beneficial role of the nanostructured materials for this reaction.

#### 4. Conclusions

The catalytic performances for the soot combustion over ceria-based catalysts mainly depend on the presence of highly reactive (100) and (110) surfaces abundant on the Ce-NC surfaces, which resulted to be the materials with the highest intrinsic activity among the ones here investigated. Furthermore high-surface area catalysts (Ce-ND, Ce-SAS) result to be less effective, thus confirming the surface-sensitivity for this reaction. Furthermore, the accessible (real) surface area plays a key role for this solid–solid reaction mediated by gas-phase oxygen. Therefore, a higher dependence of the oxidation activity on the soot-to-catalyst ratios appears for the nanostructured catalyst (Ce-NC), thus confirming its higher accessible surface area (*i.e.* more interactions between soot and catalyst) despite its very low specific surface area measured by the BET method.

It is worth mentioning that these experimental observations on powder catalysts should be confronted to the ones with the same catalyst morphologies deposited on a structured system as in [31], which considers the proper way filtered soot and layered catalyst get in contact in real DPFs. More specifically, the cake grows during filtration leaving the soot-catalyst contact only at the interface of the cake and catalyst layer, which affects the share of catalytic and non-catalytic soot oxidation inside the filter.

#### Acknowledgment

The Ministero dell'Università e della Ricerca (MIUR) (grant number: RBFR12LS6M 001) is acknowledged for sponsoring this research activity (FIRB–Futuro in Ricerca 2012).



## Appendix A. Supplementary data

Supplementary data associated with this article can be found, in the online version, at <http://dx.doi.org/10.1016/j.apcatb.2016.06.006>.

## References

- [1] E. Aneggi, C. de Leitenburg, A. Trovarelli, in: A. Trovarelli, P. Fornasiero (Eds.), *Catalysis by Ceria and Related Materials*, 2nd ed., Imperial College Press, London, 2013, pp. 565–621.
- [2] R.M. Heck, R.J. Farrauto, S.T. Gulati, *Catalytic Air Pollution Control: Commercial Technology*, 3rd ed., Wiley-VCH, Hoboken, New Jersey, 2006, pp. 518.
- [3] E.S.J. Lox, in: G. Ertl, H. Knözinger, F. Schüth, J. Weitkamp (Eds.), *Handbook of Heterogeneous Catalysis*, 2nd ed., Wiley-VCH, Weinheim, 2008, pp. 2274–2344.
- [4] D. Fino, N. Russo, G. Saracco, V. Specchia, *Powder Technol.* 180 (2008) 74–78.
- [5] A. Bueno-López, *Appl. Catal. B* 146 (2014) 1–11.
- [6] R. Burch, *Catal. Rev.* 46 (2004) 271–334.
- [7] A. Russell, W.S. Epling, *Catal. Rev. Sci. Eng.* 53 (2011) 337–423.
- [8] P. Eastwood, *Critical Topics in Exhaust Gas Aftertreatment*, Research Studies Press Ltd., Baldock, England, 2000, pp. 400.
- [9] S. Bensaid, C.J. Caroca, N. Russo, D. Fino, *Can. J. Chem. Eng.* 89 (2011) 401–407.
- [10] S. Bensaid, N. Russo, *Catal. Today* 176 (2011) 417–423.
- [11] M. Piumetti, S. Bensaid, N. Russo, D. Fino, *Appl. Catal. B* 180 (2016) 271–282.
- [12] I. Atribak, F.E. Lopez-Suarez, A. Bueno-Lopez, A. Garcia-Garcia, *Catal. Today* 176 (2011) 404–408.
- [13] S. Bensaid, N. Russo, D. Fino, *Catal. Today* 216 (2013) 57–63.
- [14] D. Fino, S. Bensaid, M. Piumetti, N. Russo, *Appl. Catal. A* 509 (2016) 75–96.
- [15] J. Oi-Uchisawa, A. Obuchi, T. Nanba, in: D. Duprez, F. Cavani (Eds.), *Handbook of Advanced Methods and Processes in Oxidation Catalysis*, Imperial College Press, 2014, pp. 25–50.
- [16] J.P.A. Neef, M. Makkee, J.A. Moulijn, *Appl. Catal. B* 8 (1996) 57–78.
- [17] P.A. Kumar, M.D. Tanwar, S. Bensaid, N. Russo, D. Fino, *Chem. Eng. J.* 207 (2012) 258–266.
- [18] E. Aneggi, D. Wiater, C. De Leitenburg, J. Llorca, A. Trovarelli, *A.C.S. Catal.* (2014) 172–181.
- [19] P. Miceli, S. Bensaid, N. Russo, D. Fino, *Chem. Eng. J.* 278 (2015) 190–198.
- [20] M. Piumetti, S. Bensaid, N. Russo, D. Fino, *Appl. Catal. B* 165 (2015) 742–751.
- [21] H.-X. Mai, L.-D. Sun, Y.-W. Zhang, R. Si, W. Feng, H.-P. Zhang, H.-C. Liu, C.-H. Yan, *J. Phys. Chem. B* 109 (2005) 24380–24385.
- [22] M. Piumetti, S. Bensaid, D. Fino, N. Russo, *Appl. Catal. B*, <http://dx.doi.org/10.1016/j.apcatb.2016.02.023>.
- [23] G. Wulff, *Z. Kristallogr. Mineral* 34 (1901) 449–530.
- [24] A.S. Barnard, *J. Phys. Chem. B* 110 (2006) 24498–24504.
- [25] P. Miceli, S. Bensaid, N. Russo, D. Fino, *Nanoscale Res. Lett.* 9 (254) (2014) 1–10.
- [26] E. Aneggi, C. de Leitenburg, J. Llorca, A. Trovarelli, *Catal. Today* 197 (2012) 119–126.
- [27] G.A. Somorjai, J. Carrazza, *Ind. Eng. Chem. Fundam.* 25 (1986) 63–69.
- [28] M. Ruitenbeek, A.J. van Dillen, F.M.F. de Groot, I.E. Wachs, J.W. Geus, D.C. Koningsberger, *Top. Catal.* 10 (2000) 241–254.
- [29] G.I. Golodets, *New developments in selective oxidation*, in: G. Centi, F. Trifirò (Eds.), *Studies in Surface Science and Catalysis*, 55, Elsevier, Amsterdam, 1990, p. 693.
- [30] A. Bueno-López, K. Krishna, M. Makkee, J.A. Moulijn, *J. Catal.* 230 (2005) 237–248.
- [31] V. Di Sarli, G. Landi, L. Lisi, A. Saliva, A. Di Benedetto, *Appl. Catal. B* (2016), <http://dx.doi.org/10.1016/j.apcatb.2016.01.073>.